ChemElectroChem

Research Article
doi.org/10.1002/celc.202200341

Chemistry Europe
European Chemical Societies Publishing

www.chemelectrochem.org

Electrochemical Reduction of CO_2 on Au Electrocatalysts in a Zero-Gap, Half-Cell Gas Diffusion Electrode Setup: a Systematic Performance Evaluation and Comparison to an H-cell Setup**

Shima Alinejad,[a] Jonathan Quinson,[b] Gustav K. H. Wiberg,[a] Nicolas Schlegel,[a] Damin Zhang,[a] Yao Li,[c] Sven Reichenberger,[c] Stephan Barcikowski,[c] and Matthias Arenz*[a]

Based on H-cell measurements, gold (Au) is one of the most selective catalysts for the CO_2 reduction reaction (CO_2RR) to CO. To ensure a high dispersion, typically small Au nanoparticles (NPs) are used as a catalyst. However, the preparation of small Au NPs based on conventional synthesis methods often requires the use of surfactants such as polyvinylpyrrolidone (PVP). Here, a systematic evaluation of the performance of laser-generated, surfactant-free Au NPs for the CO_2RR in a gas diffusion electrode (GDE) setup was presented and the results were compared to investigations in an H-cell configuration. The GDE setup supplied a continuous CO_2 stream at the electrode-electrolyte interface to circumvent CO_2 mass transport limitations encountered in conventional H-cells. The influence of the catalyst loading and the effect of PVP were investigated. By comparing the two screening methods, that is GDE and H-cell measurements, it was shown that the performance of the same catalyst could be substantially different in the two environments. In the GDE setup without liquid electrolyte-catalyst interface a higher reaction rate, but lower faradaic efficiency was determined. Independent of the setup, the presence of PVP favoured the hydrogen evolution reaction (HER). However, in the GDE setup PVP was more detrimental for the performance than in the H-cell.

Introduction

The electrochemical reduction of CO_2 (CO_2RR) into value-added products such as fuels and chemicals is considered an important contribution to curbing the use of fossil fuels and consequently diminishing atmospheric emissions of CO_2.[1] In the presence of an active and selective heterogeneous or homogeneous catalyst, CO_2 can be reduced towards carbon monoxide, formate, methanol, and other higher-value carbon-coupled products.[2,3] These products can be used as feed-stocks for chemical synthesis or converted into hydrocarbon fuels.[4] Among these products, carbon monoxide (CO) is one of the main target products of CO_2RR because syngas (H_2 and CO) is widely used in current industrial processes.[5] Achieving a high activity and selectivity is crucial for the technological and economic viability of the CO_2 electroreduction process. Low cell overpotentials ($|\eta_{cell}| < 1$ V), a CO-related current density of $j_{CO} > 150$ mA cm^{-2} and faradaic efficiency (FE) for CO ($FE_{CO} > 75$ %) are required for the economic viability of the CO_2RR[6] and remain a challenge even after almost two decades of research.[7–9] The origin of the low current densities reported cannot solely be attributed to the low performance of the used CO_2 electroreduction catalysts but also can be related to the employed screening method used for the catalytic testing itself. The most common catalyst screening method for CO_2RR is based on H-cell experiments in which the CO_2 reactant gas is dissolved in an aqueous bicarbonate-based electrolyte.[10] In such a setup, the low solubility of the CO_2 reactant gas in aqueous solutions (~35 mM at 298 K and 1 atm pressure)[9] causes mass transport limitations for the preferred CO product, whereas the reactant for the unfavored evolution of H_2 gas (i.e. water) is not mass transport limited. Therefore, in traditional testing configurations, the total measured current densities are substantially lower than the commercially relevant current densities ($j_{tot} > 200$ mA cm$_{geo}^{-2}$).[11] As a consequence, several different setups have been introduced that overcome CO_2 mass

[a] Dr. S. Alinejad, Dr. G. K. H. Wiberg, N. Schlegel, Dr. D. Zhang, Prof. M. Arenz
University of Bern
Department of Chemistry, Biochemistry and Pharmaceutical Sciences
Freiestrasse 3, 3012 Bern, Switzerland
E-mail: matthias.arenz@unibe.ch

[b] Dr. J. Quinson
University of Copenhagen
Department of Chemistry
Universitetsparken 5, 2100 Copenhagen Ø, Denmark

[c] Y. Li, Dr. S. Reichenberger, Prof. S. Barcikowski
University of Duisburg-Essen
Technical Chemistry I and Center of Nanointegration Duisburg-Essen (CENIDE), Universitätsstraße 7, Essen, North Rhine-Westphalia, 45141, Germany

[**] A previous version of this manuscript has been deposited on a preprint server (DOI: https://doi.org/10.33774/chemrxiv-2021-1 t50s-v3)

Supporting information for this article is available on the WWW under https://doi.org/10.1002/celc.202200341

© 2022 The Authors. ChemElectroChem published by Wiley-VCH GmbH. This is an open access article under the terms of the Creative Commons Attribution Non-Commercial NoDerivs License, which permits use and distribution in any medium, provided the original work is properly cited, the use is non-commercial and no modifications or adaptations are made.

© 2022 The Authors. ChemElectroChem published by Wiley-VCH GmbH

source: https://doi.org/10.48350/178570 | downloaded: 17.2.2023

21960216, 2022, 12, Downloaded from https://chemistry-europe.onlinelibrary.wiley.com/doi/10.1002/celc.202200341 by Universität Bern, Wiley Online Library on [09/02/2023]. See the Terms and Conditions (https://onlinelibrary.wiley.com/terms-and-conditions) on Wiley Online Library for rules of use; OA articles are governed by the applicable Creative Commons License

transport limitations by supplying a continuous CO_2 stream at the electrode-electrolyte interface in GDE flow electrolyzers.[6,12,13] The design of GDE setups can be sub-divided into microfluidic designs with a flowing catholyte[14–16] and zero-gap electrolyzers[17–21] where a gas diffusion layer (GDL), catalyst and polymer exchange membrane are combined as one unit without presence of a liquid electrolyte separating the catalyst layer from the polymer exchange membrane. As a result, zero-gap electrolyzers are also known as polymer electrolyte membrane (PEM) electrolyzers, catholyte-free, or gas-phase electrolyzers. There are several advantages of zero-gap electrolyzers over microfluidic designs: pressurizing the reactant and product flows is relatively simple, and there is no need to separate the product from the catholyte. Furthermore, because these devices are comparable to PEM water electrolyzers, they are easy to scale up to the commercial scale and build the massive stacks that are required.[22] However, zero-gap electrolyzers suffer from CO_2 reduction selectivity toward desired products due to the lack of an electrolyte between the catalyst layer and polymer exchange membrane.[17,23]

Yet, as indicated previously, also the available catalysts still limit the CO_2RR performance. According to H-cell measurements, Au is one of the most selective catalysts for CO_2RR to CO.[24] In conventional synthesis methods, such as the chemical reduction of precursors[25] and wet impregnation,[26] the presence of stabilizers, ligands, and reducing agents and/or support is necessary for the synthesis of the catalyst. Typically, surfactants and capping agents are used for the preparation of small colloidal Au NPs.[27] Polymeric materials, mainly polyvinylpyrrolidone (PVP), are applied as capping and/or stabilizing agents for synthesizing NPs in the liquid phase.[28] Using PVP in colloidal synthesis leads to NPs with controlled composition and structural features. Depending on the synthetic conditions, PVP can play the role(s) of a surface stabilizer, growth modifier, nanoparticle dispersant, and/or reducing agent. The amphiphilicity and the molecular weight of PVP can affect NP growth and morphology by providing different solubility in diverse solvents, preferential growth of selected crystal facets, and even access to kinetically controlled growth conditions.[29] In this respect, it must be mentioned that synthetic surfactants have negative impacts on the environment such as ruining aquatic microbial populations, damaging aquatic life, reducing photochemical energy conversion efficiency of plants, and detrimentally affecting waste-water treatment processes. Considering that roughly 60% of the global usage of surfactants, which is over 15 million tons, winds up in the aquatic environment, it is imperative to act urgently for finding alternative ways of shaped-control catalyst synthesis.[30] In addition, albeit surfactants ease the route of shaped-control catalyst synthesis, depending on the interaction between the surfactants and the surface of the NPs, surfactants can strongly influence NPs catalytic properties.[31–33] The protection of the catalyst surface by surfactants can lead to both catalyst poisoning and deactivation[34] or improved selectivity for the desired products.[33,35,36] For instance, if the binding between the capping agent and metal surface is too strong, the reactivity of the metal NPs remarkably diminishes. On the other hand, the presence of the ligands can also electronically alter a too-strong adsorption strength (enthalpy) of products and educts optimal or block undesired adsorption configurations and thereby affect the oxidation of specific functional groups in the reactant molecule.[33,35,36] To study which of this broad spectrum of influences and possible cross-correlations a surfactant induces on the catalytical properties of surfactant-free NPs are required.[33] Considering the superior role of the shape-controlled NPs in electrocatalysis, the most critical issue is to either establish a synthesis strategy for surfactant-free nanoparticles or a post-treatment strategy to remove the capping agents and surfactants from the particle surfaces without any alteration of particle size, morphology, etc. For surfactant or capping agent removal from the surface of NPs, various strategies have been developed in the last years,[37–39] however, a facile method to clean the surface of the NPs remains challenging. As an example, thermal treatment can lead to the loss of the surface orientation and agglomeration of the NPs.[40] Generally, the simple removal of PVP molecular impurities considerably alters nanoparticle size, shape, and formation kinetics[41] and it requires energy and time-consuming steps.[42]

In this study, we used pulsed laser ablation in liquids (PLAL) to directly synthesize surfactant-free Au colloidal NPs,[33,43,44] here referred to as Au-PVP-free NPs. Afterward, the Au-PVP-free NPs batch was split into two parts. One batch was kept as is, while PVP was added to the other batch, here referred to as Au-PVP NPs. Consequently, the Au-PVP-free and Au-PVP colloidal NPs come from the same source and they have the same particle size avoiding the influence of particle size effects during the measurements. This way, the laser-generated Au NP can act as a surfactant-free reference catalyst similar to previous studies.[45]

One of the objectives of the presented work was to establish the catalyst performance of Au-PVP-free NPs generated by pulsed laser ablation as a promising method for large-scale production of surfactant-free Au colloids for CO_2RR. Furthermore, we investigated the influence of PVP on the catalytic performance of the Au NPs. In the next step, we looked at the influence of the reaction environments, i.e., a GDE setup with high reactant mass transport and a conventional H-cell with limited CO_2 mass transport. We employed our recently introduced GDE setup[10,46] that originally has been designed for the application in fuel cell research[47] and can be characterized with respect to its application for the CO_2RR as a zero-gap, half-cell GDE setup. In this setup, a humidified CO_2 stream is continuously fed through the GDE cell, adjacent to the catalyst film to circumvent CO_2 mass transport limitations. In our GDE cell, as in other zero-gap designs, the catalyst layer is not directly in contact with any liquid electrolyte, but instead a membrane electrolyte separates the working electrode (catalyst layer) compartment from an electrochemical cell that houses the liquid electrolyte, the CE, and the RE. Therefore, pressurizing the reactant and product flows is easier as there is no need for product separation from the catholyte. Thus, not only this setup offers the advantage of providing a three-electrode setup, but also because of the similarity of this design to PEM fuel cell technologies, it is easier to be scaled up to the commercial

© 2022 The Authors. ChemElectroChem published by Wiley-VCH GmbH

21960216, 2022, 12, Downloaded from https://chemistry-europe.onlinelibrary.wiley.com/doi/10.1002/celc.202200341 by Universität Bern, Wiley Online Library on [09/02/2023]. See the Terms and Conditions (https://onlinelibrary.wiley.com/terms-and-conditions) on Wiley Online Library for rules of use; OA articles are governed by the applicable Creative Commons License

scale.[12] To characterize the performance in the GDE setup, we performed the same potentiostatic CO_2 electrolysis experiments in the GDE and an H-cell setup and compared the results.

Experimental Section

Chemicals, materials, gases, and instruments

For the preparation of the catalyst ink, isopropanol (IPA, 99.7+%, Alfa Aesar) and a Nafion ionomer (D1021, 10 wt% in H_2O, EW 1100, Fuel Cell Store) were used. For the electrolyte preparation, the membrane activation, and the GDE cell cleaning the ultrapure Milli-Q water (resistivity >18.2 MΩ cm, total organic carbon (TOC)< 5 ppb) from a Milli-Q system (Millipore IQ7000) was used. Potassium hydroxide (KOH, Merck) and Potassium bicarbonate ($KHCO_3$, ACS grade, Sigma-Aldrich) were used for the electrolyte preparation. An Anion exchange membrane (Sustainion® X37-50 Grade RT Membrane, with a dry thickness of 50 μm thick, Dioxide Materials) and gas diffusion layers (GDL) with a microporous layer (MPL, H23C8, 200 μm thick @ 1 MPa, Freudenberg) and without a microporous layer (H23, 170 μm thick @ 1 MPa, Freudenberg) were employed in the GDE measurements. H_2 (99.999%), CO_2 (99.999%), and calibration standard gas from (Carbagas, Switzerland) were used in the electrochemical measurements. A gas chromatograph (Model 8610C, SRI Instruments) equipped with a thermal conductivity detector (TCD) and a flame ionization detector (FID) coupled to a methanizer were used to detect hydrogen and carbon monoxide, respectively. To avoid damage of the GC column, the outlet gas of the CO_2RR cell was passed by a drying tube to remove the excess water (Cole-Parmer Drierite, Fisher Scientific) before reaching the sample loop of the GC. The gas flow rate was controlled and measured during the CO_2 electrolysis by two flow meters (universal flow meter 7,000 GC by Ellutia and Q-Flow 140, FLQ-CTSS-BK-M, CONTREC AG).

Synthesis of Au-PVP-free and Au-PVP colloidal nanoparticles

In order to generate the Au colloidal NPs, a ns-laser system (EdgeWave IS-400-L) and a continuous-flow ablation chamber were used[48] (Figure S1a–b). For generating the particles, the laser beam was focused onto the bulk Au target surface (0.5 mm thick foil, 99.99% purity, AGOSI) and moved by a galvanometric scanner system (Sunny S-8210D) at 2 m s^{-1} scan speed in a rectangular pattern. To focus the laser onto the target, the scanner was equipped with an F-Theta lens (f = 100 mm). The working distance between the lens (surface) and the target was set to 115 mm to maximize nanoparticle productivity. Milli-Q water (>18.2 MΩ cm) containing 500 μM NaCl was pumped through the ablation chamber with a flow rate of 100 mL min^{-1} during ablation. The added NaCl in micromolar concentration is a well-known size-quenching agent for laser-generated colloidal gold nanoparticles where the chloride improves the electrostatic stabilization and hence quenches nanoparticle growth directly during laser synthesis.[49] A nanoparticle productivity of 1 g h^{-1} which is in line with previous studies on laser ablation with nanosecond-pulsed IR lasers[48] was calculated from the ablation time and a differential weighting of the target before and after ablation. With the given flow rate, the gained concentration of Au nanoparticles was 160 mg L^{-1}. To remove residual size fractions larger than 10 nm, the laser-generated colloids were continuously size-separated by a tubular bowl centrifuge (CEPA LE GP) with a rotation speed of 40,000 rpm and a colloid volume flow rate of 50 mL min^{-1}. The desired small size fraction of the Au-PVP-free colloid was obtained with a concentration of 37.5 mg L^{-1} measured by inductively coupled plasma-mass spectrometry (ICP-MS) and used for further experiments. The main advantage of using a tubular bowl centrifuge is that a large volume of the colloid can continuously be processed without interruption.[48] The hydrodynamic particle size distribution of the initial laser-generated Au colloid and the small fraction after continuous centrifugation determined by analytical disc centrifugation are shown in Figure S1c–d. The Au-PVP-free colloid batch was split into two parts. One part was kept as is (Au-PVP-free), while a 0.9 mM PVP solution (Arcos Organics, 3500 g mol^{-1}) was added to 6 L Au colloid under constant mixing (Au-PVP, 0.15 mM). The primary particle size of the separated particles is verified by transmission electron microscopy (TEM) and small-angle x-ray scattering (SAXS) (Figure 1).

Preparation of the catalyst ink

13.2 mL of the colloidal Au suspension (=0.5 mg of Au) and 2.6 μL of the 10 wt.% Nafion dispersion was mixed with 13.2 mL of IPA. The glass vial containing the mixture was sonicated in an ultrasonic bath for 15 min. For the ink preparation, two types of ionomer dispersions, i.e., a Nafion ionomer and an Anion ionomer (Sustainion XA-9 Alkaline Ionomer 5% in ethanol, Dioxide Materials) were examined (Figure S2 and S3). The Anion ionomer caused particle agglomeration especially for the Au-PVP-free ink, resulting in a color change of the colloidal dispersions from red to purple. Results of ultraviolet–visible (UV-Vis) spectroscopy (Figure S4) indicate that adding the Nafion ionomer to the Au-PVP-free or Au-PVP colloidal suspensions does not cause any interaction with the NPs as the UV-Vis peak position does not shift. Therefore, Nafion ionomer was chosen for the ink preparation. The UV-Vis spectra recorded upon adding Anion ionomer into the ink (Figure S5), indicate that the presence of the PVP prevents the interaction between ionomer and NPs.

Preparation of the catalyst film

For the preparation of the catalyst films, a vacuum filtration setup was used (Figure S6). In this setup, a cylindrical reservoir with a cross-sectional area of 1.76 cm^2 was placed on top of the GDL, which was positioned onto a fritted glass filter. All this was placed on a collecting bottle. The reservoir was filled with 9.45 or 2.36 mL of ink and afterward, vacuum was applied with the help of a Schlenk line pump. By slowly sucking the ink through the GDL, a homogenous catalyst layer was obtained, which was dried overnight in air. The theoretically obtained Au loading of the thus prepared GDE is 100 $\mu g_{Au}\,cm_{geo}^{-2}$ (for 9.45 mL of ink) and 25 $\mu g_{Au}\,cm_{geo}^{-2}$ (for 2.36 mL of ink). As the colloidal Au NPs were not supported, a loss of particles during the vacuum filtration process was expected. Therefore, for the determination of the real catalyst loading, inductively coupled plasma-mass spectrometry (ICP-MS) of freshly prepared and dissolved samples (see description below) was performed (Table 1). As the vacuum filtration process and the film preparation of the Au-PVP GDEs were the same as for the Au-PVP-free GDEs, we expect the same loading for Au-PVP GDEs. However, because of the presence of PVP in the Au-PVP GDEs, it was not possible to perform a reliable ICP-MS analysis. In

Table 1. Determined Au loadings of Au-PVP-free GDEs.

Type of GDE	Theoretical Au loading [$\mu g_{Au}\,cm_{geo}^{-2}$]	Measured Au loading based on ICP-MS analysis [$\mu g_{Au}\,cm_{geo}^{-2}$]
Au-PVP-free	25	10±1
Au-PVP-free	100	1

© 2022 The Authors. ChemElectroChem published by Wiley-VCH GmbH

21960216, 2022, 12, Downloaded from https://chemistry-europe.onlinelibrary.wiley.com/doi/10.1002/celc.202200341 by Universität Bern, Wiley Online Library on [09/02/2023]. See the Terms and Conditions (https://onlinelibrary.wiley.com/terms-and-conditions) on Wiley Online Library for rules of use; OA articles are governed by the applicable Creative Commons License

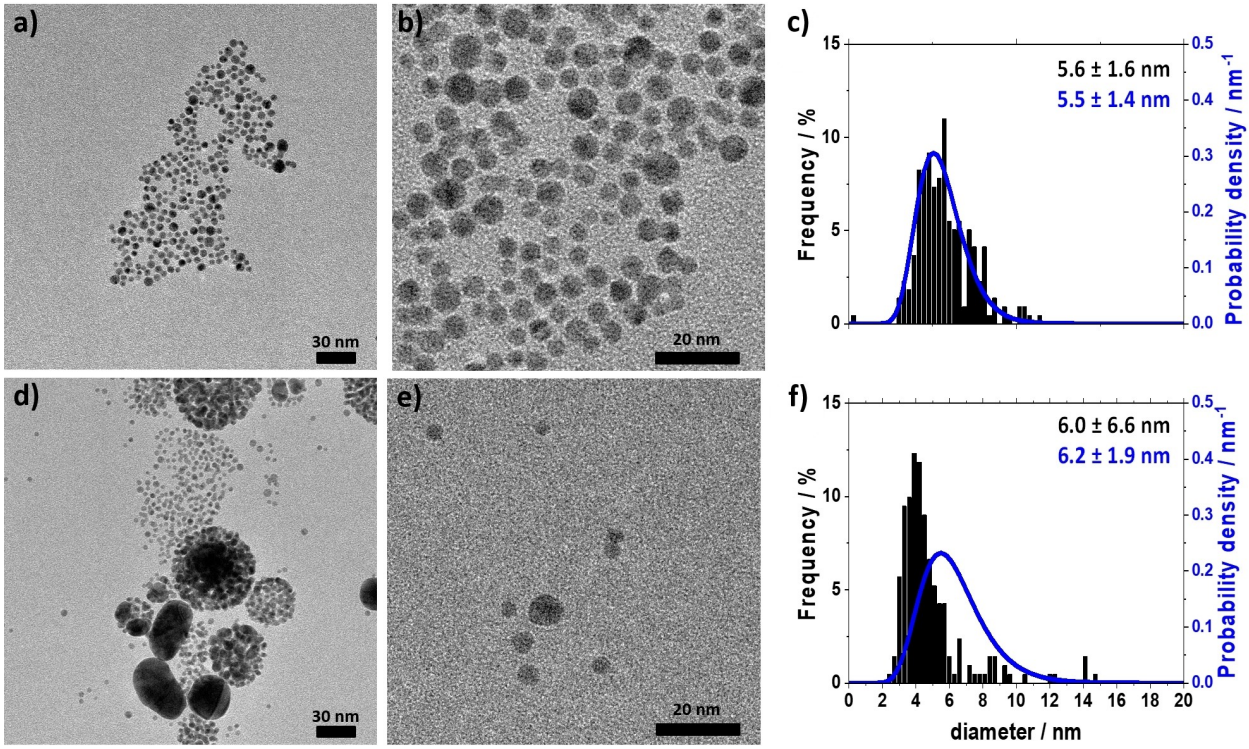

Figure 1. Representative TEM micrographs recorded at different magnifications showing Au-PVP-free (a and b), and Au-PVP (d and f) colloidal NPs. The particle size distribution derived from the TEM (black, left Y-axis), and SAXS analysis (blue, right Y-axis) for Au-PVP-free (c), and Au-PVP (f) colloid NPs.

the following, the samples will be defined by the catalyst loading as evaluated by ICP-MS.

Preparation of working electrodes (WE)

From the GDE, a WE with a circular diameter of Ø 3 and 5 mm was punched and inserted into the GDE setup and H-cell, respectively. For the GDE setup, one GDL without and one with MPL (micro porous layer) (Ø 2 cm) was used, respectively. To assemble the GDE, a hole of Ø 3 mm in the center that was filled with the Ø 3 mm GDE, and an activated Anion membrane (Ø 2 cm) was placed between the upper cell body (polytetrafluoroethylene, PTFE) and the lower cell body (stainless steel). For the activation of the Anion membrane, it was previously immersed in 1 M KOH for 24 h and thereafter punched into circles with a diameter of 2 cm. The punched and activated membranes were stored in 1 M KOH. Before assembling the membrane into the GDE setup, it was thoroughly rinsed with ultrapure Milli-Q water and thereafter dried with precision wipes (Kimtech science). For the preparation of the WE for the H-cell, a rectangular piece (0.8 cm × 3 cm) of a GDL with an MPL was used. The backside and the edges of the electrode were masked with Teflon tape thus leading to an exposed surface area of Ø 5 mm, where the punched Ø 5 mm GDE was placed. Although glassy carbon is more common as a WE for H-cell measurements, here we used a GDL to have the same porosity and properties as the GDE setup. So doing, we can have a fairer comparison between the results of the GDE setup and the H-cell setup.

Preparation of the GDE setup

Our recently introduced GDE setup was employed in this study.[10,46,47] As described above, the WE in the form of a GDE was placed on top of the flow field in the stainless-steel lower cell body and an activated Anion exchange membrane was placed on top of the GDE to separate the liquid electrolyte from the catalyst layer. The PTFE upper cell body was placed above the Anion membrane and pressed to the lower cell body by means of a stainless-steel clamp and then it was filled with 15 mL of 2 M KOH (pH ≈ 14). A silver/silver chloride electrode (Ag/AgCl, 3 M KCl, VWR, double junction design) and a gold wire were used as a reference electrode (RE) and a counter electrode (CE), respectively. For improving the reproducibility of the measurements, the CE was placed inside a glass capillary with a glass frit on the bottom to avoid the trapping of gas bubbles in the Teflon cell. All potentials in this study are referred to the RHE potential based on the following formula $E_{RHE} = E_{Ag/AgCl} + E^{0}_{Ag/AgCl} + 0.059 \times pH$ (in volts). We used the pH values of bulk electrolyte, 0.5 M $KHCO_3$ in the H-cell (pH ≈ 7.2) and 2 M KOH in the GDE setup (pH ≈ 14), for the RHE conversions. Moreover, the resistance between the WE and RE and the applied electrode potentials was monitored online using an AC signal (5 kHz, 5 mV). The cleaning of the cell was same as our previous works.[50,51] A glass bubbler was connected to the gas inlet of the lower cell body to humidify the gas. During electrolysis, a humidified CO_2 stream (16 mL min^{-1}) was continuously fed through the inlet of the GDE setup to transport the gaseous products from the outlet of the GDE setup to the sample loop of the GC.

Preparation of the H-cell setup

A custom-built gas-tight H-type glass cell with a proton exchange membrane (Nafion 117, Sigma Aldrich) separating the catholyte and the anolyte was used in this study. Both cathodic and anodic compartments were filled with 30 mL of 0.5 M $KHCO_3$ (pH ≈ 7.2) electrolyte. The described WE (section 2.5) and a single junction Ag/AgCl (saturated KCl, Pine Research) as RE were placed in the cathodic compartment. A Pt foil (0.8 cm × 2 cm) as CE was placed in

© 2022 The Authors. ChemElectroChem published by Wiley-VCH GmbH

21960216, 2022, 12, Downloaded from https://chemistry-europe.onlinelibrary.wiley.com/doi/10.1002/celc.202200341 by Universität Bern, Wiley Online Library on [09/02/2023]. See the Terms and Conditions (https://onlinelibrary.wiley.com/terms-and-conditions) on Wiley Online Library for rules of use; OA articles are governed by the applicable Creative Commons License

the anodic compartment. Prior to the CO_2 electrolysis, both cathodic and anodic compartments were saturated with CO_2 (13 mL min^{-1}) for 30 min. The CO_2 flow enabled the transport of gaseous products from the headspace of the catholyte to the sample loop of the GC.

CO_2 electrolysis experiment

Potentiostatic CO_2 electrolysis experiments were carried out for 1 h at the selected applied electrode potentials using a potentiostat (ECi-200, Nordic Electrochemistry Aps). The outlet gas of the cell was continuously flowing through the gas chromatograph (GC), and at a certain period of time, every 10 min, the analysis of gaseous products was carried out by online GC triggered by the potentiostat. The GC was calibrated before measurements with a calibration standard gas mixture (Carbagas, Switzerland) containing all products (CO and H_2). A fresh WE was used for each experiment to prevent the possible influence of catalyst layer degradation on the product distribution. The control file program of the GC and a representative chromatogram of a GC analysis are given in figure S7 and S8.

Equations (2.1) or (2.2) were used to calculate the faradaic efficiency (FE) for a given gaseous product (i) in both GDE and H-cell setups:

$$FE_i = \frac{i_i}{i_{total}} = \frac{C_i{}^* v^* z^* F^* P}{10^6 R^* T^* i_{total}} \tag{2.1}$$

Or

$$FE_i = \frac{i_i}{i_{total}} = \frac{C_i{}^* v^* z^* F}{10^6 V_m{}^* i_{total}} \tag{2.2}$$

where i_i (A) represents the partial current for the conversion of CO_2 into the product (i), C_i (Vol%) is the concentration of product (i) measured by online GC, ν (L s^{-1}) is the gas flow rate as determined by a flow meter (7000 Ellutia), z is the number of electrons involved in the formation of the particular product, F represents Faraday's constant (96500 C mol^{-1}), $V_m = RT/P$ is a molar volume, P is the pressure in the electrochemical cell headspace, T is the temperature. Here we consider $V_m = 22.4$ L mol^{-1} which is the molar volume of an ideal gas at ambient condition, and i_{total} (A) the total current at the time of the injection of the gas into the sample loop of the GC. Therefore, all gaseous products can be detected, and their respective FE (%) can be determined. It is worth mentioning that the sum of all products partial current densities (j_i) should be equal to total measured current.

Ultraviolet-Visible (UV-Vis) extinction spectroscopy

The Au-PVP-free and Au-PVP colloidal suspension and catalyst ink before and after Anion and Nafion ionomer addition were measured by UV/Vis extinction spectroscopy (Thermo Scientific GENESYS 10S UV-Vis Spectrophotometer) in a glass cuvette with 10 mm path length.

Inductively coupled plasma-mass spectrometry (ICP-MS)

A WE with a circular diameter of Ø 3 and loaded with freshly prepared Au-PVP-free and Au-PVP catalysts (GDEs) was placed in a glass test tube. The test tube was kept in a water bath at 60 °C under vigorous stirring. After the addition of 5 mL aqua regia into the tube, the latter was quickly closed for 1 hour with the help of a stopper. In this way, the reaction of the hydrochloric acid (HCl 37 %, Grogg Chemie) and nitric acid (HNO_3 65 %, Merk) could take place inside while containing the vapor inside to quantitatively dissolve the Au NP film on the GDE. The resulting solution was diluted by factors of 100, 50, and 30 with 3 % HNO_3 and was then fed into a NExION 2000 ICP-MS instrument (PerkinElmer) to determine the Au mass loading of the electrodes.

Transmission electron microscopy (TEM)

The Au NP colloids were dropped on a TEM grid and were analyzed using a Jeol 2100 TEM microscope operated at 200 kV. The size of the nanoparticles was evaluated using the ImageJ software and the average diameter was evaluated from at least 200 individual nanoparticles from different micrographs to ensure that they are representative for the sample.

Small-angle X-ray scattering (SAXS)

The colloidal Au NPs were also characterized by SAXS following the general procedure and methods detailed elsewhere.[52] In short, the Au NP colloids were placed in dedicated capillaries and measured using a SAXSLab instrument at the Niels Bohr Institute at the University of Copenhagen. The background used for measurements was MilliQ water.

Scanning electron microscopy and energy-dispersive X-ray spectroscopy

The cross-sectional characterization of the prepared catalyst films of 50 $\mu g_{Au}\, cm_{geo}{}^{-2}$ of Au-PVP-free and Au-PVP GDEs was carried out with scanning electron microscopy (SEM) imaging. The analysis was conducted with a Zeiss Gemini 450 scanning electron microscope with both InLens secondary electron detectors. An accelerating voltage of 2 kV and a current of 200 pA were applied at a working distance of 4 mm. The use of imaging coupled to energy-dispersive X-ray analysis (EDX) analysis made it possible to track the stabilization of Au NPs on top of the GDL. The AZtec 4.2 software (Oxford Instruments) was used to acquire EDX spectra and surface mappings of the GDEs. An acceleration voltage of 20 kV and a current of 200 pA was applied at a working distance of 8.5 mm.

Raman spectroscopy

Raman spectra were collected by a LabRAM HR800 confocal microscope (Horiba Jobin Yvon, Germany). The spectra were acquired using a 100× objective lens (MPLFLN, Olympus, Japan) and a 532 nm laser source for excitation (16 mW, torus 532, Laser Quantum, UK). The backscattered light was dispersed by an 1800 line/mm grating and subsequently detected by a 1024× 256 pixel CCD detector at a temperature of −59 °C. For calibration, a silicon wafer standard (520.6 cm^{-1}) was used.

Results and Discussion

As mentioned in the introduction one of the objectives of this study was to compare the performance of Au-PVP-free NPs and Au-PVP NPs towards the CO_2RR. The representative TEM micrographs of the as-prepared Au-PVP-free and Au-PVP NPs, and particle size distributions derived from the TEM and SAXS analysis for these two Au NP colloids are given in Figure 1. As expected, (both samples are aliquotes of the same batch) a

© 2022 The Authors. ChemElectroChem published by Wiley-VCH GmbH

21960216, 2022, 12, Downloaded from https://chemistry-europe.onlinelibrary.wiley.com/doi/10.1002/celc.202200341 by Universität Bern, Wiley Online Library on [09/02/2023]. See the Terms and Conditions (https://onlinelibrary.wiley.com/terms-and-conditions) on Wiley Online Library for rules of use; OA articles are governed by the applicable Creative Commons License

similar particle size of ~6 nm is observed within the error margin for both samples. Yet, a very high deviation of about 6 nm was observed for the PVP-containing sample. This deviation was linked to particularly large black "chunks" observed in the TEM images (Figure 1d) that were included in the size determination to avoid systematic exclusion of potentially large Au NPs and led to a tail to larger particle sizes in the particle size histogram. Yet, it is more likely that these "chunks" can be attributed to dried PVP on the TEM grids since the Au-PVP colloidal suspension potentially still contained free PVP. SAXS measurements were additionally performed on the colloidal dispersions (without the need for drying) to validate the size distribution obtained by TEM. The volume-averaged probability density function derived from SAXS analysis indicates a narrower size distribution than evaluated by TEM when PVP was used with a size around 6.2 ± 1.9 nm, Figure 1-f. We therefore conclude that we can investigate the effect of PVP on the CO_2RR without the potential influence of a particle size effect.

In addition to the colloidal NPs, we characterized the as-prepared GDEs by SEM and EDX. In Figure 2 representative cross-sectional SEM images of the prepared GDE's including EDX mapping are shown for as-prepared Au-PVP-free and Au-PVP GDEs with a loading of 50 $\mu g_{Au}\,cm_{geo}^{-2}$. The imaging

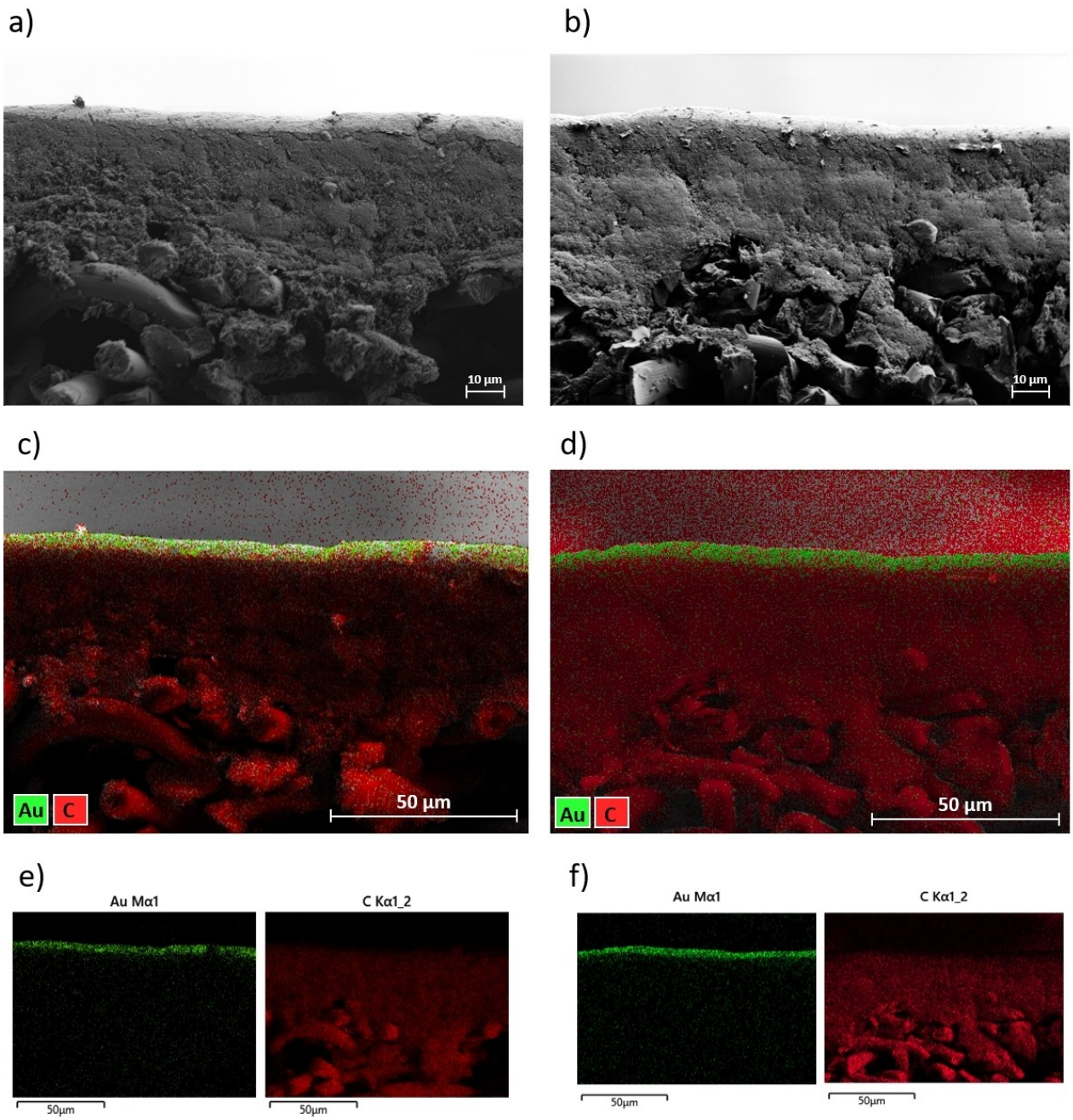

Figure 2. Representative cross-sectional SEM images (a and b) and EDX mapping (c, d, e, and f) of Au-PVP-free (a, c, and e), and Au-PVP (b, d, and f) GDEs. The Au loading was 50 $\mu g_{Au}\,cm_{geo}^{-2}$.

© 2022 The Authors. ChemElectroChem published by Wiley-VCH GmbH

21960216, 2022, 12, Downloaded from https://chemistry-europe.onlinelibrary.wiley.com/doi/10.1002/celc.202200341 by Universität Bern, Wiley Online Library on [09/02/2023]. See the Terms and Conditions (https://onlinelibrary.wiley.com/terms-and-conditions) on Wiley Online Library for rules of use; OA articles are governed by the applicable Creative Commons License

indicates that for both, the Au-PVP-free and the Au-PVP GDEs, the Au NPs are deposited on top of the MPL of the GDL and they do not permeate into the GDL.

PVP influence

Based on conventional H-cell measurements, Au is one of the most selective catalyst materials for the CO_2RR to CO.[24] Therefore, we first investigated the Au-PVP-free catalyst in an H-cell setup to establish a benchmark performance. The applied pulsed laser ablation method for generating the surfactant-free Au NPs is a well-established method that can be used for large-scale production.

For the CO_2RR testing, we chose a potential window from −0.4 to −1.0 V_{RHE}. FEs and current densities of the gaseous products obtained from the CO_2RR on an electrode with 50 $\mu g_{Au}\,cm_{geo}^{-2}$ of Au-PVP-free catalyst are shown in Figure 3. The known behavior of Au catalyst is confirmed specially for low overpotentials. At −0.4 V_{RHE} the FE (faraday efficiency) for CO (FE_{CO}) is around 98%, but only a low current of ca. 20 $mA\,cm_{geo}^{-2}$ is obversed. Decreasing the applied potential to −0.7 V_{RHE} and −1.0 V_{RHE}, the FE_{CO} decreases to 90 and 75%, respectively. At the same time the total current increases to ca. 40 and 70 $mA\,cm_{geo}^{-2}$, respectively. The decrease in FE_{CO} might be in part due to the different availability of the two different reactants CO_2 and water. Furthermore, a slight time dependence in the recorded FE_{CO} and total current density, especially at higher overpotential of −1.0 V vs RHE, is seen.

In Figures 4, we compare the influence of PVP in the H-cell setup. Clearly, the presence of the PVP leads to lower FE_{CO} and lower total current densities. For example considering the middle applied overpotential of −0.7 V vs RHE for Au-PVP-free (Figure 3b) and Au-PVP (Figure 4b), in presence of PVP the FE_{CO} decreased from 90% to 60% and the total current density decreased from 40 to 30 $mA\,cm_{geo}^{-2}$. As mentioned in the introduction, surfactants, and capping agents such as PVP are often employed in the synthesis of NPs, especially if shape-control is desired. Their use in catalysis, however, often requires their removal from the metallic surfaces without loss of surface quality.[40] Besides this practical implication, it has been shown that ligand-free Au NPs show far better agreement between theory and experiment (in a Langmuir-Hinshelwood-model reduction reaction) compared to polymer-capped Au NPs, attributed to the higher surface potential and higher accessibility of active sites.[45] As expected in presence of the PVP, the activity and selectivity of the catalyst deteriorate. It is worth noting that PVP is a hydrophilic polymer, and it can cause more water adsorption on the surface of the catalyst, resulting in more H_2 being produced. Therefore, surfactant free Au NPs are preferred catalyst for the CO_2RR. For their preparation, the pulsed laser ablation preparation method is well-established and scalable.

Catalyst screening method influence

Despite the fact, that surfactant-free Au NPs are a promising catalyst that can be synthesized in a scalable, under none of the investigated conditions, the total current densities in the H-cell setup came close to commercially relevant values (≈200 $mA\,cm_{geo}^{-2}$).[11] To increase the mass transport, we employed a zero-gap, half-cell GDE setup,[10,46] where the reactant gas does not need to be first dissolved in liquid electrolyte. To demonstrate the influence of the reaction environment, we performed the same measurements as before in the H-cell setup. The obtained FE_{CO} and current densities are shown in Figure 5 and Figure S9. It is seen that by supplying a

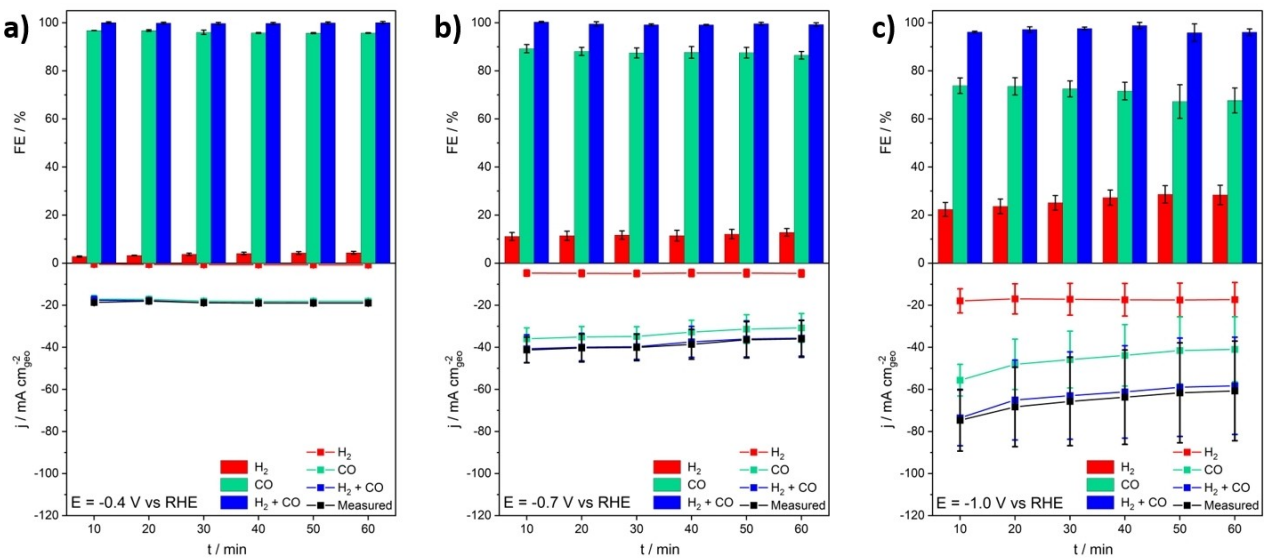

Figure 3. FEs and current densities of the gaseous products obtained from CO_2RR on 50 $\mu g_{Au}\,cm_{geo}^{-2}$ of Au-PVP-free catalyst every 10 min of 1-hour CO_2 electrolysis at applied potentials of −0.4 a), −0.7 b), and −1.0 V c) vs RHE in an H-Cell setup. The solid lines are guides for the eye to better follow the trends. The error bars indicate the standard deviation retrieved from three measurements.

© 2022 The Authors. ChemElectroChem published by Wiley-VCH GmbH

21960216, 2022, 12, Downloaded from https://chemistry-europe.onlinelibrary.wiley.com/doi/10.1002/celc.202200341 by Universität Bern, Wiley Online Library on [09/02/2023]. See the Terms and Conditions (https://onlinelibrary.wiley.com/terms-and-conditions) on Wiley Online Library for rules of use; OA articles are governed by the applicable Creative Commons License

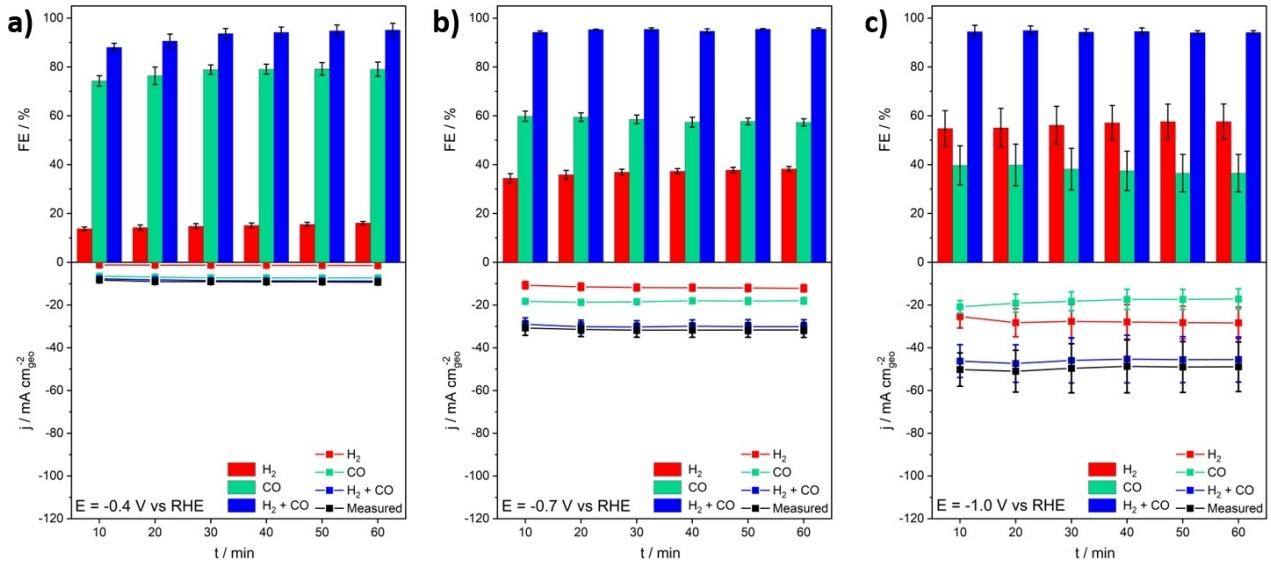

Figure 4. FEs and current densities of the gaseous products obtained from CO_2RR on 50 $\mu g_{Au}\,cm_{geo}^{-2}$ of Au-PVP catalyst every 10 min of 1-hour CO_2 electrolysis at applied potentials of −0.4 a), −0.7 b), and −1.0 c) V vs RHE in an H-Cell setup. The solid lines are guides for the eye to better follow the trends. The error bars indicate the standard deviation retrieved from three measurements.

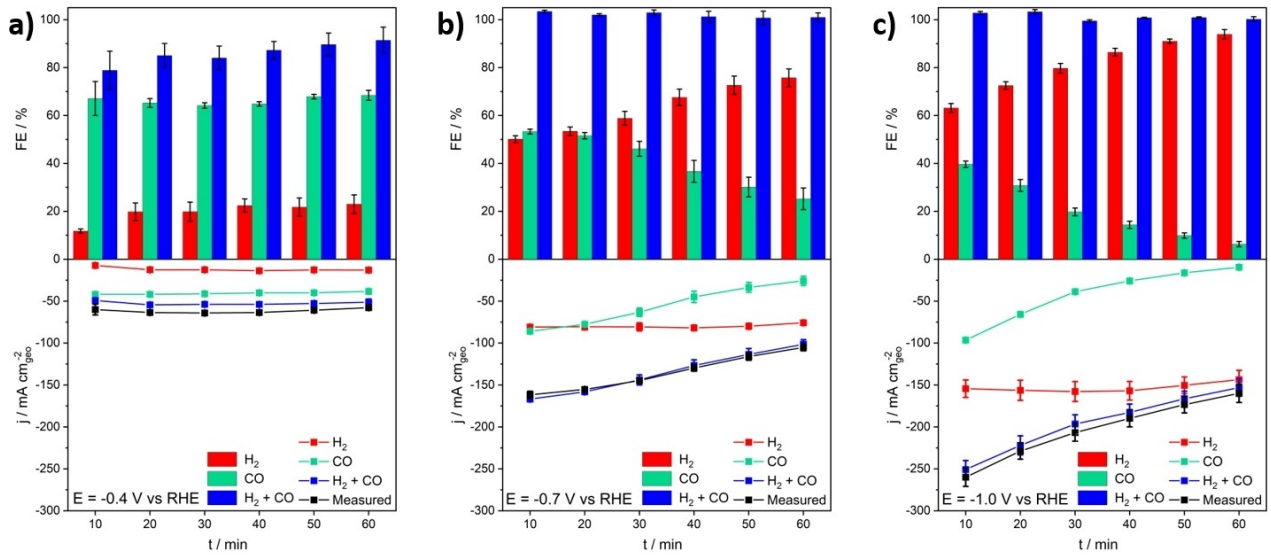

Figure 5. FEs and current densities of the gaseous products obtained from CO_2RR on 50 $\mu g_{Au}\,cm_{geo}^{-2}$ of Au-PVP-free catalyst every 10 min of 1-hour CO_2 electrolysis at different applied potentials −0.4 a), −0.7 b), and −1.0 c) V vs RHE in GDE setup. The solid lines are guides for the eye to better follow the trends.

continuous CO_2 stream through the GDL to the catalyst layer in the GDE setup, the total current densities could be increased to ca. 50, 160, and 250 mA cm_{geo}^{-2} at −0.4, −0.7 and −1.0 V_{RHE}, respectively. In the latter case, the current density achieves the industrially relevant 200 mA cm_{geo}^{-2}. However, this achievement is clearly at the expense of selectivity towards CO. With increasing total current densities, the FE_{CO} decreases from ca. 65% to 50% and 40%. Furthermore, at higher overpotentials, neither the total current densities nor the FE_{CO} are stable but decay within the 1 h of the measurement.

It has been shown previously that without the direct presence of a solid-supported electrolyte, the CO_2 reduction selectivity can be heavily penalized.[17,53] The fact that the FE_{CO} decreases with increasing overpotential and concomitant increasing total current density seems to be a general, independent of the reaction environment. However, the fact that the higher current densities one can achieve in the GDE setup are penalized by a lower selectivity towards CO (FE_{CO}), could indicate that the selectivity, in general, depends on the current density as well as the overpotential. At the same time, the poor selectivity of the Au-PVP-free NPs in the GDE setup as

© 2022 The Authors. ChemElectroChem published by Wiley-VCH GmbH

21960216, 2022, 12, Downloaded from https://chemistry-europe.onlinelibrary.wiley.com/doi/10.1002/celc.202200341 by Universität Bern, Wiley Online Library on [09/02/2023]. See the Terms and Conditions (https://onlinelibrary.wiley.com/terms-and-conditions) on Wiley Online Library for rules of use; OA articles are governed by the applicable Creative Commons License

compared to the H-cell setup might be attributed to carbonate precipitation.[10] With a direct contact of liquid electrolyte to the catalyst surface,[53] such precipitates are washed out, but not in catholyte-free GDE setups under the chosen conditions. It is therefore worth mentioning that under current conditions the achieved total current density of more than 200 mA cm_{geo}^{-2} (Figure 5-c) this current is mainly attributed to the HER. Therefore, the GDE setup needs to be optimized to alleviate the selectivity and stability of the catalyst over time and transport precipitations away from the catalyst layer. Nevertheless, catalyst screening in H-cell setups is questionable as the achieved current densities are far from industrial scales and current density and selectivity might be related.

To complete our comparison, we investigated the influence of PVP in the GDE setup (Figure 6 and Figure S10). As for the case of the Au-PVP-free catalyst, the FE_{CO} is deteriorated in the absence of direct aqueous electrolyte in the GDE setup. As in the H-cell setup, in the presence of the PVP a lower total FE in the beginning of the 1-hour CO_2 electrolysis was observed in GDE setup. However, the detrimental effect of PVP on the FE is substantially more severe than in the H-cell setup. Our electrochemical results show that in the presence of PVP at all overpotentials, especially at lower one (−0.4 V_{RHE}), the total FE is substantially lower than in the measurements of the Au-PVP-free catalyst. It has to mention that for samples with a total FE of less than 100%, a longer GC analysis as well as ionic exchange chromatography on the liquid electrolyte were performed for detecting the other possible products. However, no other product components other CO and H_2 could be detected.

A possible explanation for the low total FE might be parasitic currents due to the reduction of the surfactant. Especially at −0.4 V vs RHE, the overall current is very small, therefore small parasitic currents due to surfactant reduction have a substantial influence on the total FE. The results show a constant increase in total FE over the time of the electrolysis as well as by increasing the applied potential from −0.4 to 1.0 V vs RHE. This indicates an "electrochemical cleaning" of the Au-PVP catalyst, i.e., the removal of the PVP from the catalyst surface. Such a process would be in line with the decreasing cell resistance observed during the measurement (Figure S11). To determine if the PVP is only partially or completely removed from the catalyst surface, we performed Raman spectroscopy before and after CO_2RR. The Raman spectra of (1) PVP powder, (2) Au-PVP ink on mica film, (3) the blank GDL, (4) pristine Au-PVP catalyst loaded with 50 μg_{Au} cm_{geo}^{-2} on a GDL, and (5) resembling (4) after 1 hour of electrolysis at −1.0 V_{RHE} are shown in the Figure S12. Although we could detect a sharp PVP signal in the Raman spectrum of the Au-PVP ink on a mica film, due to the lack of enough Au-PVP catalyst on the GDL, we were not even able to detect a clear PVP signal in the pristine sample.

Loading effect in GDE setup

After scrutinizing the influence of PVP, we also investigated the influence of the catalyst loading in the GDE setup. In Figure S13 the results obtained from a GDE setup with 10 μg_{Au} cm_{geo}^{-2} of Au-PVP-free catalyst are shown and in Figure 7 we compare the different loadings of the Au-PVP-free catalyst in the GDE setup. It is seen that by decreasing the loading of the catalyst from 50 to 10 μg_{Au} cm_{geo}^{-2}, the selectivity towards CO worsens. However, the change in current densities is almost negligible. This result might indicate that the selectivity does not depend on the absolute current density, but more precise on the current density per metal loading. However, simply increasing the metal loading will only be beneficial if the complete catalyst layer is active. In the case of unsupported NPs as in this study, higher loadings while maintaining an accessible catalyst layer is difficult. However, supporting of the NPs onto a porous carbon

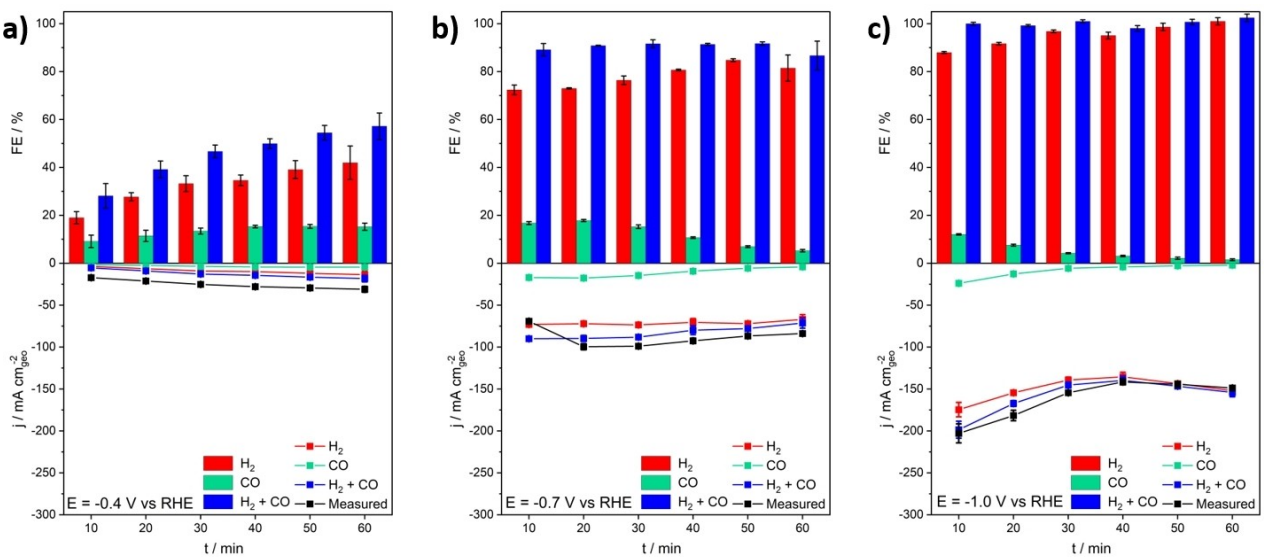

Figure 6. FEs and current densities of the gaseous products obtained from CO_2RR on 50 μg_{Au} cm_{geo}^{-2} of Au-PVP catalyst every 10 min of 1-hour CO_2 electrolysis at different applied potentials −0.4 a), −0.7 b), and −1.0 c)V vs RHE in GDE setup. The solid lines are guides for the eye to better follow the trends.

© 2022 The Authors. ChemElectroChem published by Wiley-VCH GmbH

21960216, 2022, 12, Downloaded from https://chemistry-europe.onlinelibrary.wiley.com/doi/10.1002/celc.202200341 by Universität Bern, Wiley Online Library on [09/02/2023]. See the Terms and Conditions (https://onlinelibrary.wiley.com/terms-and-conditions) on Wiley Online Library for rules of use; OA articles are governed by the applicable Creative Commons License

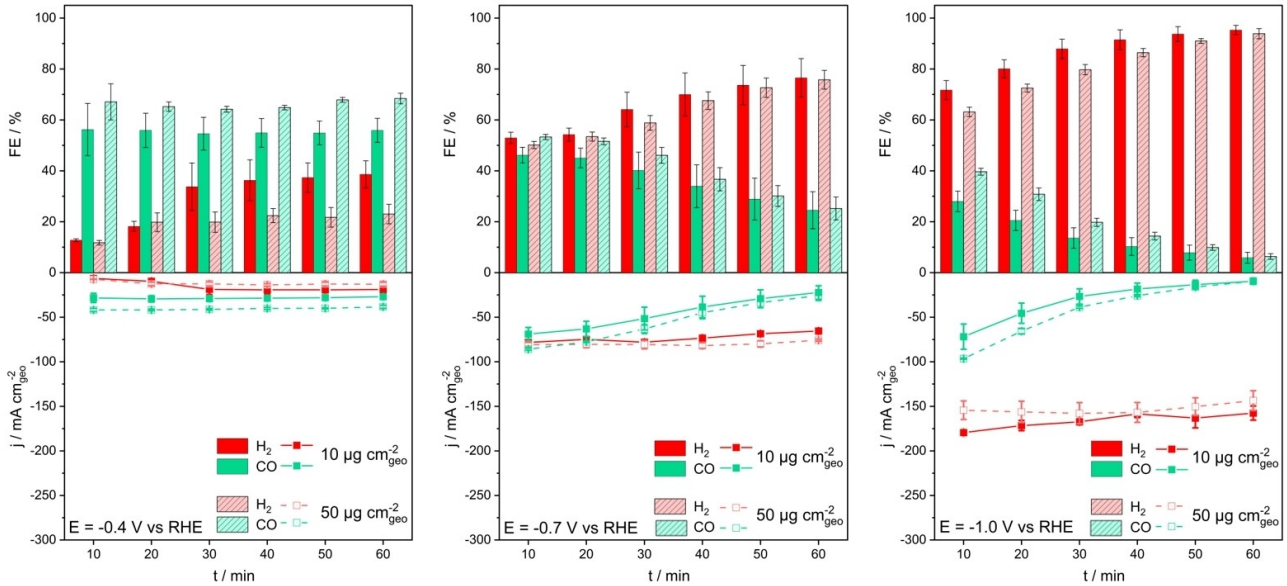

Figure 7. FEs and current densities of the gaseous products obtained from CO_2RR on 10 and 50 $\mu g_{Au}\,cm_{geo}^{-2}$ of Au-PVP-free catalyst every 10 min of 1-hour CO_2 electrolysis at different applied potentials in the GDE setup. The solid lines are guides to better follow the trends.

might be a solution to circumvent this drawback. In addition, we performed CO_2 electrolysis on a blank GDL (H23C8) for one hour at −0.7 V vs RHE in the GDE setup, Figure S14, and we observed that balank GDL causes HER. By decreasing the loading of the catalyst from 50 to 10 $\mu g_{Au}\,cm_{geo}^{-2}$, we will have more contribution from the blank GDL. Therefore we observe more HER and the selectivity towards CO worsens.

Conclusion

In this work, we systematically investigated the influence of three experimental variables on the performance of Au-based catalysts for the electrochemical CO_2RR, i.e., first the absence or presence of a polymer surfactant, second the influence of the reaction environment (testing setup), and third the influence of the catalyst loading. The influence of surfactants was investigated by adding surfactants to a surfactant-free colloidal suspension of Au NPs. It was shown that the presence of PVP inhibits CO as a reduction product and it favors the HER. To maximize selectivity towards CO, and activity of the catalyst, considering the total current density, the use of surfactants such as PVP in the catalyst synthesis should be avoided. In order to avoid the usage of surfactants we used pulsed laser ablation method for generating shaped and sized-control surfactant-free Au NPs. We demonstrated that the Au-PVP-free NPs which are generated by pulsed laser ablation method not only are very selective toward CO production during the CO_2RR, but also their generation method is scalable for higher quantities. For mimicking commercially relevant conditions for the CO_2RR by using a zero-gap, half-cell GDE setup enables high mass transport conditions, we observed that technologically relevant total current densities higher than 200 mA cm_{geo}^{-2} could be obtained which was not the case in an H-cell setup. However, the high current densities were achieved at the expense of a lower selectivity towards CO. The sensitivity of the catalyst to PVP inhibition seemed more critical in a GDE setup than it in an H-cell. The results also indicated that the selectivity of the CO_2RR towards CO depends on the current density per metal loading, but by increasing the catalyst loading from 10 to 50 $\mu g_{Au}\,cm_{geo}^{-2}$ only negligible improvements in the current densities are achieved. This result calls for effective catalyst benchmarking procedures and will be a key to develop further CO_2RR catalysts for industrial applications.

Acknowledgements

This work was supported by the Swiss National Science Foundation (SNSF) via project No. 200021_184742. Jonathan Quinson acknowledges the European Union's Horizon 2020 research and innovation program under the Marie Skłodowska-Curie grant agreement No. 840523 (CoSolCat). S. B. Simonsen and L. Theil Kuhn, Technical University of Denmark, are thanked for access to TEM. The Niels Bohr Institute, University of Copenhagen, Denmark, is thanked for access to SAXS equipment, in particular J. K. K. Kirkensgaard. Open access funding provided by Universitat Bern.

Conflict of Interest

The authors declare no conflict of interest.

© 2022 The Authors. ChemElectroChem published by Wiley-VCH GmbH

21960216, 2022, 12, Downloaded from https://chemistry-europe.onlinelibrary.wiley.com/doi/10.1002/celc.202200341 by Universität Bern, Wiley Online Library on [09/02/2023]. See the Terms and Conditions (https://onlinelibrary.wiley.com/terms-and-conditions) on Wiley Online Library for rules of use; OA articles are governed by the applicable Creative Commons License

Data Availability Statement

The data that support the findings of this study are openly available in Chemrxiv at 10.33774/chemrxiv-2021-1t50s-v3, reference number 2021.

Keywords: Au nanoparticles · CO_2 electroreduction · Gas diffusion electrodes · Polyvinylpyrrolidone surfactant · Zero-gap design

[1] D. T. Whipple, P. J. A. Kenis, *J. Phys. Chem. Lett.* **2010**, *1*, 3451.
[2] Y. Hori, K. Kikuchi, S. Suzuki, *Chem. Lett.* **1985**, *14*, 1695.
[3] Y. Hori, in *Mod. Asp. Electrochem.*, Springer, New York, NY, **2008**, pp. 89–189.
[4] G. Centi, S. Perathoner, *Catal. Today* **2009**, *148*, 191.
[5] H. Hu, M. Liu, Y. Kong, N. Mysuru, C. Sun, M. D. J. Gálvez-Vázquez, U. Müller, R. Erni, V. Grozovski, Y. Hou, P. Broekmann, *ACS Catal.* **2020**, *10*, 8503.
[6] S. Verma, Y. Hamasaki, C. Kim, W. Huang, S. Lu, H. R. M. Jhong, A. A. Gewirth, T. Fujigaya, N. Nakashima, P. J. A. Kenis, *ACS Energy Lett.* **2018**, *3*, 193.
[7] S. Hernández, M. A. Farkhondehfal, F. Sastre, M. Makkee, G. Saracco, N. Russo, *Green Chem.* **2017**, *19*, 2326.
[8] S. Verma, B. Kim, H. R. M. Jhong, S. Ma, P. J. A. Kenis, *ChemSusChem* **2016**, *9*, 1972.
[9] A. J. Martín, G. O. Larrazábal, J. Pérez-Ramírez, *Green Chem.* **2015**, *17*, 5114.
[10] M. D. J. Gaìlvez-Vaìzquez, P. Moreno-García, H. Xu, Y. Hou, H. Hu, I. Z. Montiel, A. V. Rudnev, S. Alinejad, V. Grozovski, B. J. Wiley, M. Arenz, P. Broekmann, *ACS Catal.* **2020**, *10*, 13096.
[11] T. Burdyny, W. A. Smith, *Energy Environ. Sci.* **2019**, *12*, 1442.
[12] B. Endrődi, G. Bencsik, F. Darvas, R. Jones, K. Rajeshwar, C. Janáky, *Prog. Energy Combust. Sci.* **2017**, *62*, 133.
[13] S. Jovanovic, R. Krause, A. Lüken, J. Ackermann, S. Merz, P. Jakes, R.-A. Eichel, J. Granwehr, *J. Electrochem. Soc.* **2020**, *167*, 086505.
[14] C. M. Gabardo, A. Seifitokaldani, J. P. Edwards, C. T. Dinh, T. Burdyny, M. G. Kibria, C. P. O'Brien, E. H. Sargent, D. Sinton, *Energy Environ. Sci.* **2018**, *11*, 2531.
[15] S. Ma, R. Luo, J. I. Gold, A. Z. Yu, B. Kim, P. J. A. Kenis, *J. Mater. Chem. A* **2016**, *4*, 8573.
[16] J. J. Lv, M. Jouny, W. Luc, W. Zhu, J. J. Zhu, F. Jiao, *Adv. Mater.* **2018**, *30*, 1.
[17] Y. C. Li, D. Zhou, Z. Yan, R. H. Gonçalves, D. A. Salvatore, C. P. Berlinguette, T. E. Mallouk, *ACS Energy Lett.* **2016**, *1*, 1149.
[18] I. Merino-Garcia, E. Alvarez-Guerra, J. Albo, A. Irabien, *Chem. Eng. J.* **2016**, *305*, 104.
[19] D. M. Weekes, D. A. Salvatore, A. Reyes, A. Huang, C. P. Berlinguette, *Acc. Chem. Res.* **2018**, *51*, 910.
[20] W. Lee, Y. E. Kim, M. H. Youn, S. K. Jeong, K. T. Park, *Angew. Chem. Int. Ed.* **2018**, *57*, 6883.
[21] R. B. Kutz, Q. Chen, H. Yang, S. D. Sajjad, Z. Liu, I. R. Masel, *Energy Technol.* **2017**, *5*, 929.
[22] J. B. Vennekoetter, R. Sengpiel, M. Wessling, *Chem. Eng. J.* **2019**, *364*, 89.
[23] C. Delacourt, P. L. Ridgway, J. B. Kerr, J. Newman, *J. Electrochem. Soc.* **2008**, *155*, B42.
[24] A. Goyal, G. Marcandalli, V. A. Mints, M. T. M. Koper, *J. Am. Chem. Soc.* **2020**, *142*, 4154.
[25] J. Turkevich, P. C. Stevenson, J. Hillier, *Discuss. Faraday Soc.* **1951**, *11*, 55.
[26] M. Komiyama, *Catal. Rev.* **1985**, *27*, 341.
[27] P. Suchomel, L. Kvitek, R. Prucek, A. Panacek, A. Halder, S. Vajda, R. Zboril, *Sci. Rep.* **2018**, *8*, 1.
[28] G. H. Han, S. H. Lee, M. G. Seo, K. Y. Lee, *RSC Adv.* **2020**, *10*, 19952.
[29] K. M. Koczkur, S. Mourdikoudis, L. Polavarapu, S. E. Skrabalak, *Dalton Trans.* **2015**, *44*, 17883.
[30] P. Johnson, A. Trybala, V. Starov, V. J. Pinfield, *Adv. Colloid Interface Sci.* **2021**, *288*, DOI 10.1016/j.cis.2020.102340.
[31] I. A. Safo, M. Oezaslan, *Electrochim. Acta* **2017**, *241*, 544.
[32] J. Quinson, S. Kunz, M. Arenz, *ChemCatChem* **2021**, *13*, 1692.
[33] S. Reichenberger, G. Marzun, M. Muhler, S. Barcikowski, *ChemCatChem* **2019**, *11*, 4489.
[34] J. Zhang, G. Chen, M. Chaker, F. Rosei, D. Ma, *Appl. Catal. B* **2013**, *132–133*, 107.
[35] S. T. Marshall, M. O'Brien, B. Oetter, A. Corpuz, R. M. Richards, D. K. Schwartz, J. W. Medlin, *Nat. Mater.* **2010**, *9*, 853.
[36] S. H. Pang, C. A. Schoenbaum, D. K. Schwartz, J. Will Medlin, *ACS Catal.* **2014**, *4*, 3123.
[37] P. S. Fernández, D. S. Ferreira, C. A. Martins, H. E. Troiani, G. A. Camara, M. E. Martins, *Electrochim. Acta* **2013**, *98*, 25.
[38] D. Li, C. Wang, D. Tripkovic, S. Sun, N. M. Markovic, V. R. Stamenkovic, *ACS Catal.* **2012**, *2*, 1358.
[39] M. Cargnello, C. Chen, B. T. Diroll, V. V. T. Doan-Nguyen, R. J. Gorte, C. B. Murray, *J. Am. Chem. Soc.* **2015**, *137*, 6906.
[40] F. Hasché, M. Oezaslan, P. Strasser, *ChemPhysChem* **2012**, *13*, 828.
[41] N. El Amri, K. Roger, *J. Colloid Interface Sci.* **2020**, *576*, 435.
[42] J. A. Arminio-Ravelo, J. Quinson, M. A. Pedersen, J. J. K. Kirkensgaard, M. Arenz, M. Escudero-Escribano, *ChemCatChem* **2020**, *12*, 1282.
[43] V. Amendola, D. Amans, Y. Ishikawa, N. Koshizaki, S. Scirè, G. Compagnini, S. Reichenberger, S. Barcikowski, *Chem. A Eur. J.* **2020**, *26*, 9206.
[44] V. Merk, C. Rehbock, F. Becker, U. Hagemann, H. Nienhaus, S. Barcikowski, *Landmuir* **2014**, *30*, 4213.
[45] S. Gu, J. Kaiser, G. Marzun, A. Ott, Y. Lu, M. Ballauff, A. Zaccone, S. Barcikowski, P. Wagener, *Catal. Lett.* **2015**, *145*, 1105.
[46] M. De Jesús Gálvez-Vázquez, S. Alinejad, H. Hu, Y. Hou, P. Moreno-García, A. Zana, G. K. H. Wiberg, P. Broekmann, M. Arenz, *Chimia* **2019**, *73*, 922.
[47] G. K. H. Wiberg, M. Fleige, M. Arenz, *Rev. Sci. Instrum.* **2015**, *86*, DOI 10.1063/1.4908169.
[48] S. Kohsakowski, F. Seiser, J. P. Wiederrecht, S. Reichenberger, T. Vinnay, S. Barcikowski, G. Marzun, *Nanotechnology* **2020**, *31*, DOI 10.1088/1361-6528/ab55bd.
[49] A. Letzel, S. Reich, T. Dos Santos Rolo, A. Kanitz, J. Hoppius, A. Rack, M. P. Olbinado, A. Ostendorf, B. Gökce, A. Plech, S. Barcikowski, *Langmuir* **2019**, *35*, 3038.
[50] S. Alinejad, J. Quinson, J. J. Schröder, J. J. K. Kirkensgaard, M. Arenz, *ACS Catal.* **2020**, *10*, 13040.
[51] S. Alinejad, M. Inaba, J. Schröder, J. Du, J. Quinson, A. Zana, M. Arenz, *J. Phys. E* **2020**, *2*, 024003.
[52] J. Quinson, A. Dworzak, S. B. Simonsen, L. Theil Kuhn, K. M. Ø. Jensen, A. Zana, M. Oezaslan, J. J. K. Kirkensgaard, M. Arenz, *Appl. Surf. Sci.* **2021**, *549*, DOI 10.1016/j.apsusc.2021.149263.
[53] D. A. Salvatore, D. M. Weekes, J. He, K. E. Dettelbach, Y. C. Li, T. E. Mallouk, C. P. Berlinguette, *ACS Energy Lett.* **2018**, *3*, 149.

Manuscript received: March 28, 2022
Accepted manuscript online: April 26, 2022

© 2022 The Authors. ChemElectroChem published by Wiley-VCH GmbH

21960216, 2022, 12, Downloaded from https://chemistry-europe.onlinelibrary.wiley.com/doi/10.1002/celc.202200341 by Universität Bern, Wiley Online Library on [09/02/2023]. See the Terms and Conditions (https://onlinelibrary.wiley.com/terms-and-conditions) on Wiley Online Library for rules of use; OA articles are governed by the applicable Creative Commons License